

Acoustically Actuated Flow in Microrobots Powered by Axisymmetric Resonant Bubbles

Sumit Mohanty, Yu-Hsiang Lin, Aniruddha Paul, Martin R. P. van den Broek, Tim Segers, and Sarthak Misra*

Bubble-driven microsystems inspired by the therapeutic use of microbubbles under clinical ultrasound actuation offer innovative remote manipulation in biological settings. Ultrasound-powered microrobots, benefiting from a distribution of vibrating microbubbles (1–100 μm in diameters), exhibit localized fluid flow for self-propulsion. Microbubbles also contribute to the design of acoustic metamaterials, where distributed actuation of bubbles enables exotic material properties (e.g., negative refractive index). Herein, a metamaterial-inspired microrobot design, which exploits the streaming induced by the collective oscillation of microbubble arrays (> 10), is reported. Such a large distribution of bubbles offers twofold advantages: a mesoscale microrobot allowing ease of handling and motion at a considerably low acoustic driving pressure of 50 kPa. In this work, the oscillatory amplitude of a single bubble that acts as a unit cell of the metamaterial-based microrobot is first characterized. Thereon, this amplitude is related to the flow generated by the collective vibration of all the bubbles close to the theoretically predicted resonant frequency of the bubbles. Finally, the hovering motion of the microrobot induced by the streaming and flow-assisted debris clearance is demonstrated. Such auxiliary functionalities of the microrobot can be useful for applications like contactless sample extraction in inaccessible biological environments.

The complimentary use of gas bubbles in clinical ultrasound and lab-on-a-chip devices has popularized contactless actuation by bubbles in biological microsystems.^[5] Particularly, compressible gas bubbles act like mass-spring systems inside fluids in response to incoming sound waves, which enables the propulsion in bubble-powered microrobots.^[6–9] Recent designs of bubble-driven microrobots allow controlled translation and rotation through different morphologies of the bubble-entrapping cavities in the body of the microrobot.^[10–12] However, predicting the motion of such large-bubble systems is challenging, as the flow fields around multiple gas bubbles are highly sensitive to the deviations in the cavity geometry and their arrangements.^[13] Few studies have attempted to model cross-interaction between different-sized bubbles in relatively simple scenarios (e.g., two-bubble systems), which leaves scope for new experimental methods to study the collective behavior of bubbles and improve the design of large-bubble systems.^[10,13]

There exists potential to design microrobots inspired by periodic repetition of bubbles to large numbers (≈ 10), such as that observed in metamaterials.^[14] This may enrich the acoustic microrobots with functionalities beyond localized bubble-powered propulsion.

Large-bubble systems have been studied extensively in the form of microrobots,^[10–12,15] lab-on-a-chip systems,^[16,17] clinical devices,^[18] and metamaterials.^[19–21] The majority of these

1. Introduction

Microrobots exploit diverse actuation strategies to harvest energy from remote sources (e.g., electric, magnetic, acoustic, and light) for contactless motion.^[1,2] Common actuation strategies employ magnetic flagella^[3] and acoustically resonant bubbles^[4] as active vibratory motors that microrobots exploit for self-propulsion.

S. Mohanty, Y.-H. Lin, S. Misra
Surgical Robotics Laboratory
Department of Biomechanical Engineering
University of Twente
7522 NB Enschede, The Netherlands
E-mail: s.misra@utwente.nl

 The ORCID identification number(s) for the author(s) of this article can be found under <https://doi.org/10.1002/aisy.202300465>.

© 2023 The Authors. Advanced Intelligent Systems published by Wiley-VCH GmbH. This is an open access article under the terms of the Creative Commons Attribution License, which permits use, distribution and reproduction in any medium, provided the original work is properly cited.

DOI: 10.1002/aisy.202300465

S. Mohanty
Soft Robotic Matter Group
Autonomous Matter Department
AMOLF
Science Park 104, 1098 XG Amsterdam, The Netherlands

A. Paul, M. R. P. van den Broek, T. Segers
BIOS Lab-on-a-Chip Group
Max Planck Center for Complex Fluid Dynamics
University of Twente
7522 NH Enschede, The Netherlands

S. Misra
Surgical Robotics Laboratory
Department of Biomedical Engineering
University of Groningen and University Medical Center Groningen
9713 AV Groningen, The Netherlands

microrobots use different-sized bubbles as a means to achieve steering.^[15,22] In contrast, some recent designs of microrobots use equal-sized bubbles to harness streaming-induced flow fields of adjacent bubbles to achieve various forms of motion.^[10,11,15] In a particular case, the collective oscillation of bubbles to produce motion^[15] has been inspired by the superimposition of flow fields observed in cyclic microfluidic channels that employ arrays of up to 1000 inclined bubbles.^[16,17] Likewise, periodic distribution of a large scale of bubbles (more than 5000 unit cells) has led to innovative designs of the endoscope^[18] and contactless rotors,^[23] where collective actuation of bubbles has boosted streaming-induced forces around the large-bubble system. These large-bubble systems comprise symmetric distributions of equal-sized bubbles taking inspiration from the periodic geometry in rigid metamaterials^[24] where each bubble represents a unit cell. Beyond microrobots and microfluidic devices, large-bubble systems are also commonly employed in soft metamaterials, e.g., negative-refractive index materials^[25,26] and protective coatings for submarines.^[27] Although the majority of large-bubble systems in soft metamaterials are not purposely designed to achieve motion, they open new possibilities for acoustic microrobots where the collective behavior of bubble-driven motors significantly enhances the efficiency of the propulsion. These aforementioned applications of large-bubble systems have been summarized in **Table 1**.

When driven by acoustic waves, the oscillating air–liquid interfaces produce the streaming effects described above, which leads to propulsion in bubble-based acoustic microrobots.^[22] Driving a large-bubble system with ultrasound signals produces higher net oscillatory fluid flows than the aggregate contributions localized to each individual bubble.^[19] This property arises due to a superimposition of flow fields around the individual resonant bubbles, which amplifies the flow in the large-bubble system.^[20] As a result, the actuation of such large-bubble systems can produce effects such as precise micromanipulation of nearby objects^[20] or enhanced sound absorption.^[21] This flow amplification exhibited by soft metamaterials provides a unique property of

exploiting bulk flow due to a series of oscillating bubbles in tandem, as unit cells, than relying on localized streaming-induced field around an individual bubble. This design rationale employed in metamaterials can provide a new strategy for designing more efficient microrobots.

Many studies on large-bubble systems (Table 1) typically use bubble geometries in millimeter scale and rarely go below $\approx 100 \mu\text{m}$.^[19,20] Among the examples of metamaterials and endoscopes, the body of most designs is made up of hydrophobic materials like polydimethylsiloxane, which allows selective entrapment of bubbles. Although this property promotes stable entrapment of microscale bubbles, it is not favorable in the design of microrobots. In the case of microrobots, the site-selective bubble entrapment requires surface modifications, which often turns the entire system hydrophobic.^[7,9] Our prior work described such surface-modified large-bubble systems with up to 6^[15] and 13 site-selective bubbles,^[11] which vibrate to perform different degrees of motion. However, the hydrophobicity of the entire system makes it hard to submerge in fluids as bubbles are often trapped in an uncontrolled manner at unwanted locations. The works by Aghankhani et al. show that using spherical cavities with re-entrant structures at these bubble entrapment sites provides a solution to synthesize large-bubble systems without rendering the entire system hydrophobic.^[8,28] Although the spherical cavities in these studies stabilize the bubble entrapment, an additional re-entrant structure is needed to achieve a longer bubble lifetime.

It is challenging to study the dynamics of the microbubbles with limited acquisition rates of commonly available imaging systems (e.g., charge-coupled device cameras) when the acoustic driving frequencies are of the order of 100 kHz (characteristic for $\approx 100 \mu\text{m}$ bubbles).^[29] For this reason, to study the oscillation amplitude of the entrapped microbubbles, a high-speed imaging system is required to capture the fast dynamic of the oscillating bubble. Here, a high-speed camera with a recording speed of 10 million frames per second enables the characterization of fast oscillating microbubbles.

Table 1. A synopsis of recently reported large-bubble systems. The application fields of the reported multibubble systems are categorized as microrobot, microchannel, endoscopes, and metamaterials. We report the intended application for these systems, the number of bubbles and size of the bubbles (i.e., unit cells in case of metamaterials), key features, and challenges, respectively.

Application	Number of bubbles	Size of bubbles [μm]	Key feature and challenges	
Microrobot	3	20–30	Tethered structures, bubbles exhibit coupling effect	[10]
Microrobot	4, 13	50–100	Hydrophobic, difficult to submerge	[11]
Microrobot	14	270–1300	Variable bubble size to achieve steerability	[12]
Microrobot	6	100	Hydrophobic, difficult to submerge	[15]
Microchannel	120	500	Superimposed flow, tethered to substrate	[16]
Microchannel	200	250–300	Superimposed flow, tethered to substrate	[17]
Endoscope	$\approx 10\,000$	55–120	Limited to linear bubble array, bubble dissolution	[18]
Endoscope	≈ 6200	30–200	Wireless actuation, bubble arrays fixed to tethered shaft	[23]
Metamaterial	27	3000	Large bubbles for a microstructure	[19]
Metamaterial	10 000	300	Force amplification, design restricted to planar patterns	[20]
Metamaterial	≈ 1000	3000	Intrinsically hydrophobic. For sound absorption, not motion	[21]
Metamaterial	40	50–80	Intrinsically hydrophobic. For sound absorption, not motion	[46]
Metamaterial	40	50–80	Intrinsically hydrophobic. For sound absorption, not motion	[47]

In this study, we report a new design of a bubble-powered microrobot that exploits the property of collective bubble oscillation-induced flow observed in large-bubble systems and bubble-based metamaterials. Herein, we show a microrobot with a 3D axisymmetric distribution of 18 gas bubbles that amplifies the superimposed induced flow of a single bubble due to the collective vibration of the constituent bubbles. Our work starts with an exploration of the constituent bubble-entrapped cavity, which forms the unit cell of our metamaterial-inspired design, based on the high-speed camera recordings of their oscillatory dynamics. Specifically, we characterize the different cavity openings of the single constituent bubble by comparing the oscillation amplitudes of their vibrating meniscus. Thereon, we validate our choice of cavity opening based on the different bubble lifetimes of the entrapped bubbles in these cavities. Next, we employ these constituent bubbles in an axisymmetric distribution within our microrobot, which vibrates to create a superimposed flow along a common central axis. As a comparison, we use the particle image velocimetry algorithm to characterize the flow velocity in the current design and the design of our prior work with a linear distribution of bubbles ($n = 6$).^[15] Finally, we utilize this flow to show the hovering motion of the microrobot and demonstrate its application for biological sample collection. Particularly, we demonstrate that the proposed metamaterial-based microrobot can collect dead HeLa cells and spheroids. The strategy behind our design offers the dual advantage of developing larger microrobots (up to millimeter scale) that are easy to handle while retaining the merits of fast oscillatory microscale actuation in the form of microbubbles.

2. Results and Discussion

We first describe the geometry of our acoustic metamaterial-inspired microrobot design and the bubble-entrapping cavities

that constitute the building blocks of this microrobot design (Figure 1). Second, a systematic acoustic characterization of the various cavity variants is presented, starting from the characterization of the oscillation amplitude using high-speed imaging to the relative bubble dissolution rate under constant acoustic excitation. Here, an acoustic characterization setup is described that is used for the measurement of bubble resonance frequency and subsequently the motion of the microrobot. We use a high-speed imaging camera that we employ at an acquisition rate of up to a million frames per second to monitor the fast vibrations of the bubbles in response to a range of driving frequencies around 100 kHz. Third, a theoretical discussion is presented to justify the design metric and relative acoustic response of a single bubble entrapped in different cavity designs. Fourth, we use particle image velocimetry to experimentally characterize the flow induced by the collective vibration of bubbles in the range of the acoustic resonance frequency.

Finally, we demonstrate the motion of the proposed microrobot, which exhibits a hovering behavior under acoustic actuation at a lower driving power compared to its previous design. Moreover, the hovering mechanism is tunable by the acoustic frequencies, which allow larger displacements of the microrobots compared to its body length, nearly visible under the naked eye (Figure 4a). This hovering motion in tandem with the inward flow through the body of the microrobot enables it to extract and remove dead cells (10 μm single cells and 200 μm spheroids) from the fluid in a contactless fashion (Figure 7). We envision this aforementioned functionality to find use in applications such as biological sample collection^[30] and waste remediation^[31] at the microscale.

2.1. Design and Fabrication of the Acoustic Microrobot

The acoustic microrobot is composed of six arrays, each consisting of three cylindrical cavities (length 100 μm , radius 20 μm)

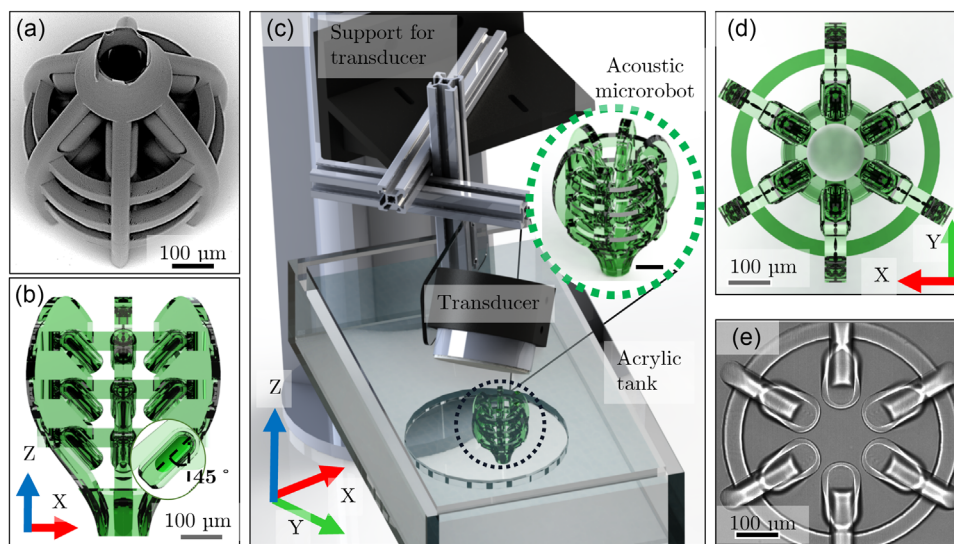


Figure 1. a) Micrograph of proposed acoustic metamaterial-inspired microrobot depicting the arrangement of cavities, with b) side view of the microrobot with the constituent cavities that entrap gas bubbles (inset). c) Schematic depicting the microrobot immersed in the acoustic characterization setup that comprises a large acrylic tank (300 mm \times 200 mm \times 100 mm) with a designated circular workspace and immersible ultrasound transducer (center frequency 110 kHz, cross-sectional diameter 60 mm, PA1954, Precision Acoustics, UK). Scale bar is 100 μm . Top view of the microrobot: d) schematic showing the rings connecting the cavities; e) Nanoscribe view of the microrobot during its fabrication.

arranged in an axisymmetric distribution around a central axis (Figure 1b). The cavities in each of the axisymmetric arrays are tilted 45° with respect to the central axis to facilitate a directional fluid flow through the body of the microrobot. The orientation of the bubbles in the microrobot is based on our prior work,^[15] which evolves from the use of tilted streaming patterns seen in various acoustofluidic microchannels.^[16,17] Another design consideration of the choice of 45° inclination is the limited printing area (500 μm × 500 μm) under direct laser writing (DLW) that affects the interaction of the streaming patterns between the two opposite bubbles. In case of the inclination larger than 45°, the length of the microrobot will increase and hence exceed the printing area (in Z-direction, Figure 1b). In another case of inclination smaller than 45°, the separation between the opposite bubble increases the width of the microrobot (in X-direction, Figure 1b), thereby reducing the magnitude of streaming-driven flow along the central axis. The six arrays are connected to each other with three concentric rings that hold the entire structure (Figure 1d,e). The microrobot is 3D printed with DLW (Nanoscribe GmbH) and is made up of IP-Dip photoresist. Details of the fabrication are given in the Experimental Section.

In contrast to our previous designs,^[11,15] the open end for each of the cavities in the microrobot is designed with a re-entrant structure to facilitate complete occupancy of the gas bubbles without any surface modification. These re-entrant structures have been investigated for longer retention of the gas bubbles as such structures promote liquid repellency, which is reported for many bubble-trapping structures.^[8,28,32,33] For the final design, the re-entrant structure consists of a radially inward protrusion of 5 μm, covering 25% of the total opening diameter (Figure S5, Supporting Information). In the following subsections, we compare the choice of this protrusion size with other potential cavity design variants as we investigate the relative oscillation amplitudes of the entrapped bubbles.

2.2. Acoustic Characterization of Gas Bubble-Filled Cavities

The acoustic characterization setup consists of an acrylic tank (300 mm × 200 mm × 100 mm), which has a circular workspace (depth 5 mm, radius 40 mm), as shown in Figure 1c. This circular workspace engraved at the bottom surface of the tank works both as a test bed for the imaging of bubble arrays and for the actuation of the microrobot. The source of acoustic actuation is an immersible ultrasonic transducer (PA1954, Precision Acoustics, UK) with a specified center frequency of 110 kHz. We first characterize the output pressure of the transducer using a calibrated needle hydrophone (NH0200, Precision Acoustics, UK). The detailed procedure of transducer calibration is described in the Experimental Section (Figure S1, Supporting Information). Due to the axisymmetric nature of the pressure response, the axial and radial distribution of the pressure is plotted in one of the radial planes of the transducer (Figure S1d, Supporting Information). The spatially resolved pressure distribution along the axial direction is uniform within 35–50 mm from the transducer at a frequency of 80 kHz. Given our concerned frequency range of driving acoustic waves (60–100 kHz)

and the cross-sectional diameter of the transducer (60 mm), the natural axial focal distance of the transducer varies between 30 and 60 mm.^[34] Thus, the transducer is positioned at an average axial working distance of ≈45 mm such that the bubble arrays are close to the natural focus of the transducer (Figure S1, Supporting Information).

Next, glass substrates with an array of constituent cylindrical cavities are used for acoustic characterization. A high-speed camera (HPV-X2, Shimadzu, Japan) is employed at a frame rate of ≈500 000 fps to record the fast vibrating meniscus of the bubbles. Details of fabrication and high-speed imaging instrumentation are described in the Experimental section. The cavities are sparsely distributed (2 mm apart on a glass substrate) and immersed in the workspace, where they are exposed to pulsed ultrasound (Figure S2, Supporting Information). A 12-cycle sinusoidal pulse ($V_{\text{peak}} = 5\text{ V}$) is applied to the transducer, which results in a peak pressure amplitude of 35 kPa (Figure 2a). The amplitude of the meniscus oscillations in response to the sinusoidal driving pulse is recorded (Figure 2b,c, Movie S1, Supporting Information). Timestamps of the bubble oscillations are recorded at 500 000 frames per second, where the maximum amplitude is observed at the ultrasound frequency of 62 kHz (Figure 2). The above-described sequences of measurements are performed with a variable step size in a range of ultrasound frequencies (5 kHz step for 50–120 kHz, 2 kHz step in 60–90 kHz, respectively), and corresponding bubble oscillation amplitudes are recorded (Figure 2e-(I)). Based on the pressure output of the transducer as measured by the hydrophone (Figure 2e-(II)), the amplitude of the bubble oscillations is normalized by the acoustic pressure (Figure 2e-(III)). Importantly, such normalization is permissible provided the oscillation amplitude varies linearly within the range of the applied driving pressure, which is verified for the range of driving amplitude to the transducer (Figure S4, Supporting Information). Finally, a comparison of the two subfigures in Figure 2e suggests that the peak oscillation amplitude shifts to a lower frequency of 62 kHz and shows a higher Q-factor upon normalization. This observation allows us to dissociate the observed acoustic resonance frequencies of most bubble-based microrobots from the inherent frequency-dependent characteristics of the transducer. In order to compare this deduced resonance frequency with the theoretical value, we discuss the formulation behind the resonance frequency of cylindrical cavities.

2.2.1. Theoretical Expression for Resonance Frequency

Previously, most bubble-powered microrobots are reported to propel with highest velocity when the applied acoustic frequency is close to the coupled natural resonance frequency (f_0) of the constituent bubbles.^[6,9,11,15] Although the natural resonance frequency provides an estimate of the resonance frequencies of cylindrical gas bubbles, it asymptotically reaches infinity when the length of the bubble approaches the length of the cavity. Furthermore, it does not take into account the influence of bubble radius.^[6,35] Hence, we formulate the resonance frequency of our constituent bubbles based on the modeling of a partially filled gas cavity by Miller et al.^[36]

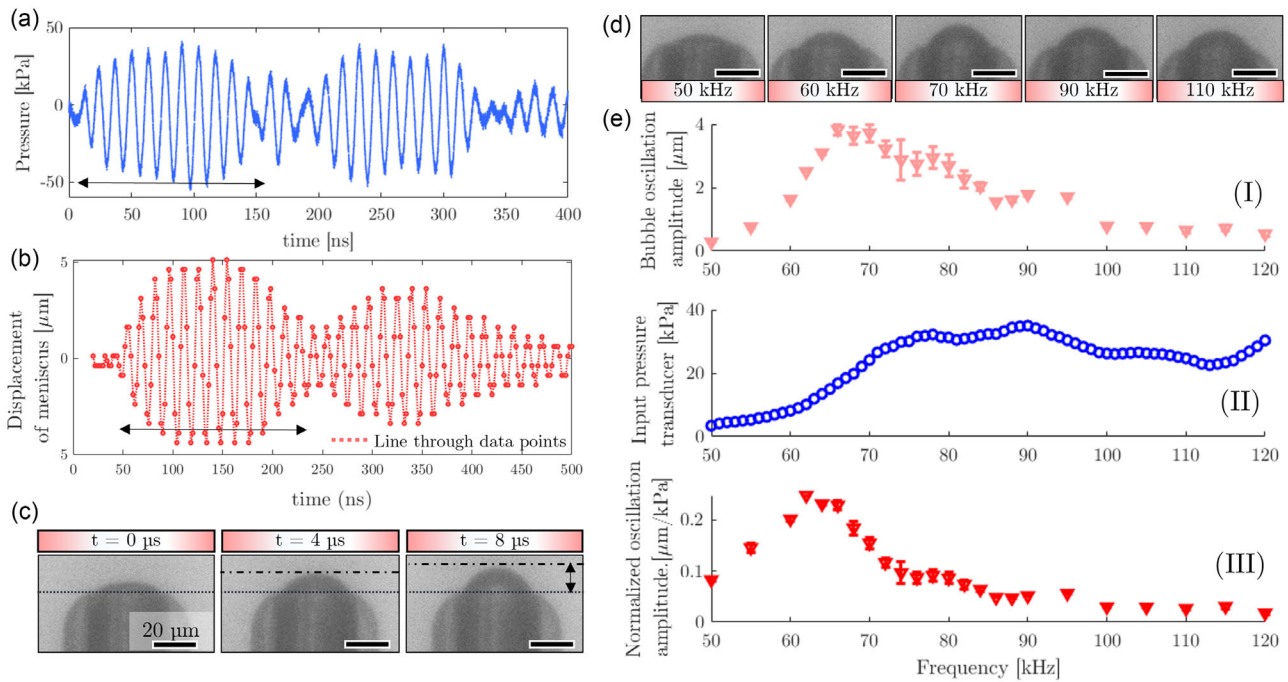


Figure 2. Ultrasound transducer and bubble characterization: a) recorded pressure signal of the transducer at 75 kHz depicting a 12-cycle burst (black arrow) followed by reflected pulses from the surrounding boundaries. b) Displacement of the meniscus of a 100 μm long cylindrical bubble driven with the pressure wave shown in (a). Data points connected to ease readability (dashed line). c) Selected frames from a high-speed movie are obtained at an ultrasound driving frequency of 62 kHz in which the maximum amplitude of oscillation (around 5 μm) is observed. d) Selected frames from high-speed movies are obtained at different ultrasound frequencies. Scale bars represent 20 μm . e) Characterization of the amplitude response of a single gas bubble as a function of frequency at a driving signal amplitude of 5 V: I) displacement of the oscillating meniscus, II) pressure output of the transducer at an axial distance of approximately 45 mm, and III) oscillation amplitude normalized to the input pressure shown in (II).

$$f_r = \frac{1}{2\pi} \left(\frac{120\pi\gamma_w L_b + 15\pi\kappa_a P_o a^2}{32\rho_w a^3 L_b + 15\pi\rho a^2 L_b (L - L_b)(1 + d_v/a)} \right)^{1/2} \quad (1)$$

where P_o denotes the ambient pressure in the bubble, κ_a the adiabatic polytropic exponent of air (≤ 1.4), ρ_w the density of the water, γ_w the surface tension of water (0.072 Nm^{-1}), and d_v the viscous boundary layer thickness, which is a function of the acoustic frequency f , given other physical parameters of (1), and can be expressed as follows

$$d_v = \sqrt{\frac{\mu_w}{\rho_w \pi f}} \quad (2)$$

where μ_w is the shear viscosity of water ($1.0 \text{ mPa}\cdot\text{s}$) and f represents the order of applied acoustic frequency. In our concerned range of acoustic frequencies, i.e., $f \approx 100 \text{ kHz}$, the term $(1 + d_v/a) \approx 1$. For the cylindrical cavities that constitute the microrobot ($L = 100 \mu\text{m}$, $a = 20 \mu\text{m}$) with completely air-filled cavities ($L_b = L = 100 \mu\text{m}$), (1) gives f_r of 73 kHz. We subject this single bubble-filled cavity to sound waves under the proposed high-speed imaging system to find the experimental value of f_r to be 62 kHz (Figure 2e). This $\approx 15\%$ difference in the two values of f_r can be attributed to the difference in geometry of the cavity design, the presence of the nearby bubbles, and the curvature of the meniscus. Next, we study the influence of re-entrant

protrusions (0–10 μm) of the cavity on the bubble oscillation amplitude and the bubble lifetime.

2.2.2. Effect of Re-Entrant Structures on Oscillation Amplitude and Lifetime of Bubble

As discussed previously, re-entrant protrusions are designed at the open end of the cavities to prevent the escape of gas bubbles without any prior hydrophobic surface treatment. We investigate protrusion designs with three different variants to the original cavity structure ($a = 20 \mu\text{m}$, $L = 100 \mu\text{m}$). Aside from the fully open cavity discussed in Section 2.2, the other two variants allow partial opening of the cavity at 50% and 75%. The cavity variations are hereon denoted by $c = 50\%$, 75%, and 100%, where c implies the proportion of bubble exposed with respect to the total inner diameter of the entrapped bubble. We record the bubble oscillation amplitudes for $c = 50\%$, 75%, 100% cavities over the same range of frequencies as in Figure 2e (Movie S1, Supporting Information). The oscillation amplitude to the applied pressure shows the highest magnitude for $c = 100\%$ whereas $\approx 5\times$ lower magnitude for $c = 50\%$ (Figure 3a) is observed. However, $c = 50\%$ could trap bubbles for at least 40 min after the experiment as opposed to $c = 100\%$, where the bubbles escape within a few minutes without any hydrophobic treatment. Thus, $c = 75\%$ is an intermediate case that

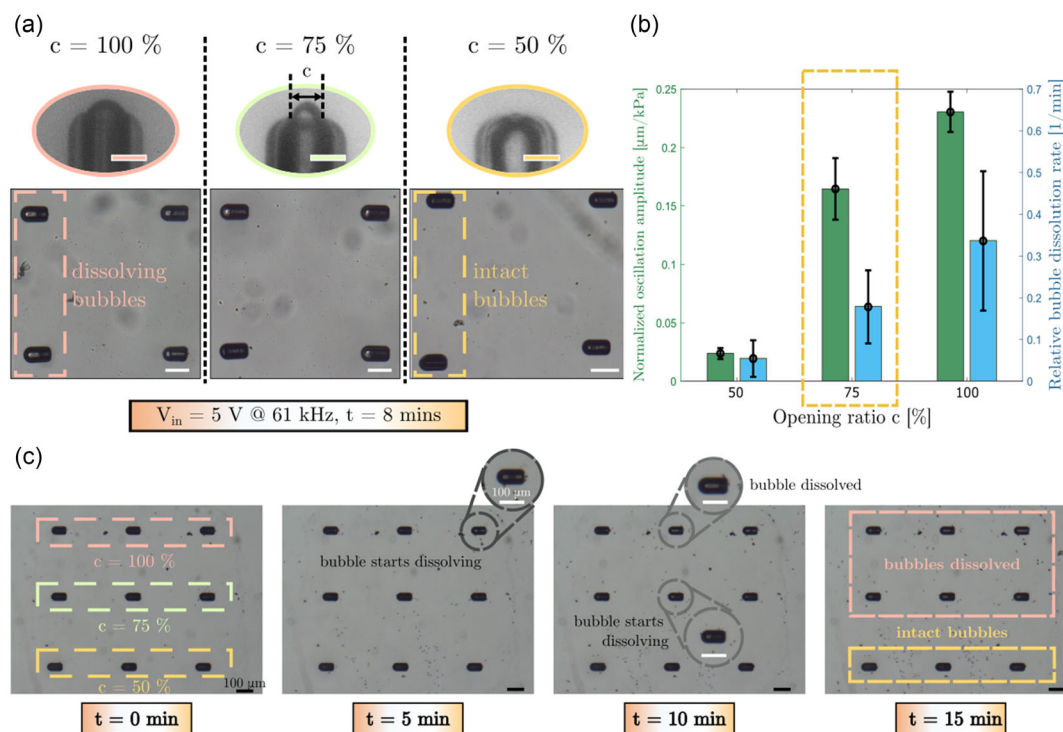


Figure 3. Characterization of different cavity openings: a) (middle row) zoomed-in views of each cavity variant, i.e., $c = 50, 75, 100\%$. Scale bars are $30\ \mu\text{m}$. (Bottom row) Snapshots of the entrapped bubbles for $c = 50, 75, 100\%$ after continuous exposure to acoustic actuation (5 V driving voltage at 61 kHz) for 8 min . Scale bars are $100\ \mu\text{m}$. b) Normalized oscillation amplitude and the relative bubble dissolution rate in three different cavity variants with openings ($c = 50, 75, 100\%$) at 61 kHz , 5 V . The relative bubble dissolution rate is determined as the average relative reduced length of the bubble after the time duration of the experiment. The desired characteristics for the cavity are high oscillation amplitude for a relatively low bubble dissolution rate. c) Timestamps of the entrapped bubbles for $c = 50, 75, 100\%$ under constant actuation at the frequency of 67 kHz and the driving pressure of around 20 kPa (transducer input voltage 5 V). Bubbles in $c = 100\%$ case start dissolving after 5 min ; $c = 75\%$ start dissolving only after 10 min ; whereas bubbles in $c = 50\%$ remain stable after 40 min of the experiment. All the scale bars in this subfigure correspond to $100\ \mu\text{m}$.

provides comparable oscillation amplitude as $c = 100\%$ while retaining the bubbles for a prolonged duration of the experiment time.

2.3. Acoustic Actuation of the Microrobot

In contrast to previous works on bubble-powered microrobots, our experimental setup configuration allows for two notable improvements in the traditional operation of microrobots in otherwise confined microfluidic workspace.^[11,15] First, the enclosed workspace offered by microfluidic setups limits the motion of microrobots as the distance traveled by these microrobots is within several body lengths as they are confined to the workspace dimensions.^[15] Second, the measurement procedure possible with the aforementioned setup (Section 2.2) avoids direct contact between the piezoelectric transducer and the workspace. With these improvements, we investigate the motion of an acoustic microrobot, when immersed in a large acrylic tank and exposed to sound waves from a contactless transducer (Figure 4a). Moreover, the overall footprint of the microrobot ($\approx 500\ \mu\text{m} \times 500\ \mu\text{m} \times 500\ \mu\text{m}$) makes it nearly visible to the naked eye and thereby easy to handle while retaining the powerful vibratory response of microscale bubbles. We begin our investigation with a study

on the streaming response of the bubbles that constitute the microrobot.

2.3.1. Experimental Investigation of Acoustic Streaming-Induced Flow

We immerse the microrobot into the acrylic tank such that it is accessible within an engraved circular workspace with the transducer focused at a distance of 45 mm to the center of the workspace. The transducer is driven with acoustic frequencies in the $50\text{--}100\text{ kHz}$ range, and the streaming of injected tracer particles around the microrobot is to visualize the flow. Although the particles exhibit streaming around the microrobot broadly within the $60\text{--}90\text{ kHz}$ range, the strongest streaming is observed at 67 kHz and 77 kHz , which is in the same range of the measured resonance frequency of a single bubble (Figure 2e-(I)). Importantly, the streaming of particles suggests a flow direction where particles enter the broader opening of the microrobot from all directions and are ejected from the opposite narrower end (Movie S3, Supporting Information). This acoustically induced flow creates a suction effect that allows the microrobot to stand up and presume a vertical orientation at 67 kHz (Figure 4b, Movie S3, Supporting Information). We use this vertical orientation of

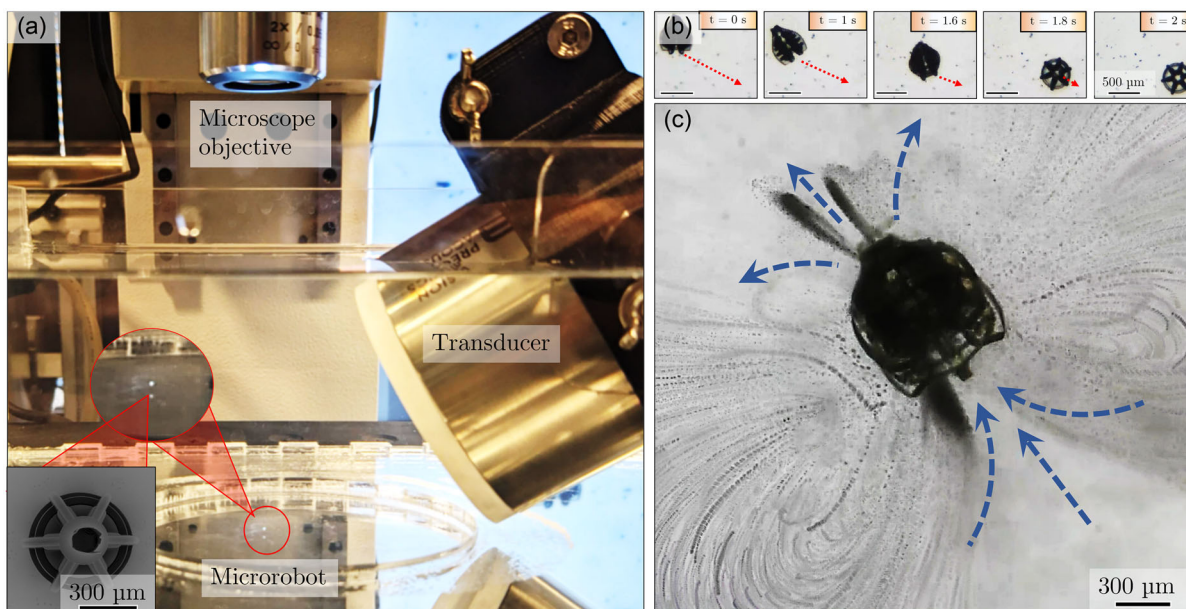


Figure 4. Motion of the acoustic microrobot: a) acoustic actuation setup showing the transducer immersed in an acrylic tank, focusing sound waves at the microrobot (inset). b) Timestamps of the microrobot assuming vertical orientation under acoustic actuation at 67 kHz (Movie S3, Supporting Information). c) Superimposed time-lapse showing the acoustic streaming pattern around the microrobot with blue arrows depicting the streaming direction.

the microrobot shown in Figure 4b to investigate its hovering motion over switching acoustic frequencies in subsequent sections. Notably, the streaming pattern of particles around the microrobot due to high-frequency flow fields extends several body lengths beyond the footprint of the microrobot (Figure 4c). This flow field strengthens the advantage behind mesoscale robots ($\approx 500\text{--}700\ \mu\text{m}$) where much smaller microbubbles ($\approx 100\ \mu\text{m}$) locally produce a high Reynolds number region around the microrobots.^[37] This localized flow field allows microrobots to move through the otherwise viscous Stoke's regime that is defined for their dimension.

2.3.2. Flow Velocity Characterization

The underlying concept of the metamaterial-inspired acoustic microrobot is the enhanced streaming caused by the collective contribution of microstreaming patterns generated by each bubble. This allows the microrobot to generate stronger streaming-driven propulsive forces with significantly lower driving voltage to the ultrasound transducer. To support this argument, we compare the flow velocity at the inlet side of microrobots from our prior work on microrobot,^[15] which comprises 6 microbubbles distributed in a similar manner to the current design with 18 microbubbles. The microrobots are driven under the same condition at 65 kHz with the driving voltage amplitude of 20 V (Figure 5a). We analyze the flow velocity at the inlet side (Figure 5a) using the particle image velocimetry algorithm (PIVlab toolbox, MATLAB)^[38] and determine the peak velocity by analyzing the particle velocity along the sectional line perpendicular to the flow direction (Figure 5b, Movie S3, Supporting Information). The peak velocity extracted from the flow analysis shows that the maximal flow velocity in the 6-bubble-microrobot

is $0.99\ \text{mm s}^{-1}$, whereas the flow velocity of the 18-bubble-microrobot is $1.77\ \text{mm s}^{-1}$, which is a 79% increase in peak velocity magnitude (Figure 5c). As we observe overall higher particle velocities along A–A' (Figure 5c), we then integrate the velocity magnitude along this line as the metric for comparing the efficiency of the streaming intensity. The integral of the velocity magnitude of the 6-bubble microrobot is $6.98 \times 10^{-3}\ \text{mm s}^{-1}$, whereas that of the 18-bubble-microrobot is $3.06 \times 10^{-2}\ \text{mm s}^{-1}$, showing an approximate fivefold increase. This measurement suggests that a large-bubble system with higher number of constituent bubbles can generate stronger flow at the same driving powers. Our finding could lead to the evolution of other microrobots that exist in the same length scale^[12] which typically require high-voltage radio frequency amplifiers to sustain propulsive forces due to lower intensity of streaming-driven forces.

2.3.3. Hovering Motion in Remote Environments

Next, we continue to explore the response of the acoustic microrobot in the range of 60–90 kHz, where it presumes a vertical orientation at 65–70 kHz, and shows streaming behavior (Movie S3, Supporting Information). In this vertical orientation, switching acoustic frequencies causes the microrobot to hover around the workspace. Although the microrobot continues to hover within the 74–77 kHz range of frequencies (Movie S4, Supporting Information), it moves faster at the driving frequency of around 67 kHz with the amplitude of the driving pressure around 50 kPa (Figure 6a), similar to the dominant streaming observed at this frequency.

Besides, a previous evaluation of single bubble-entrapped cavities ($c = 75\%$, Movie S2, Supporting Information) demonstrates

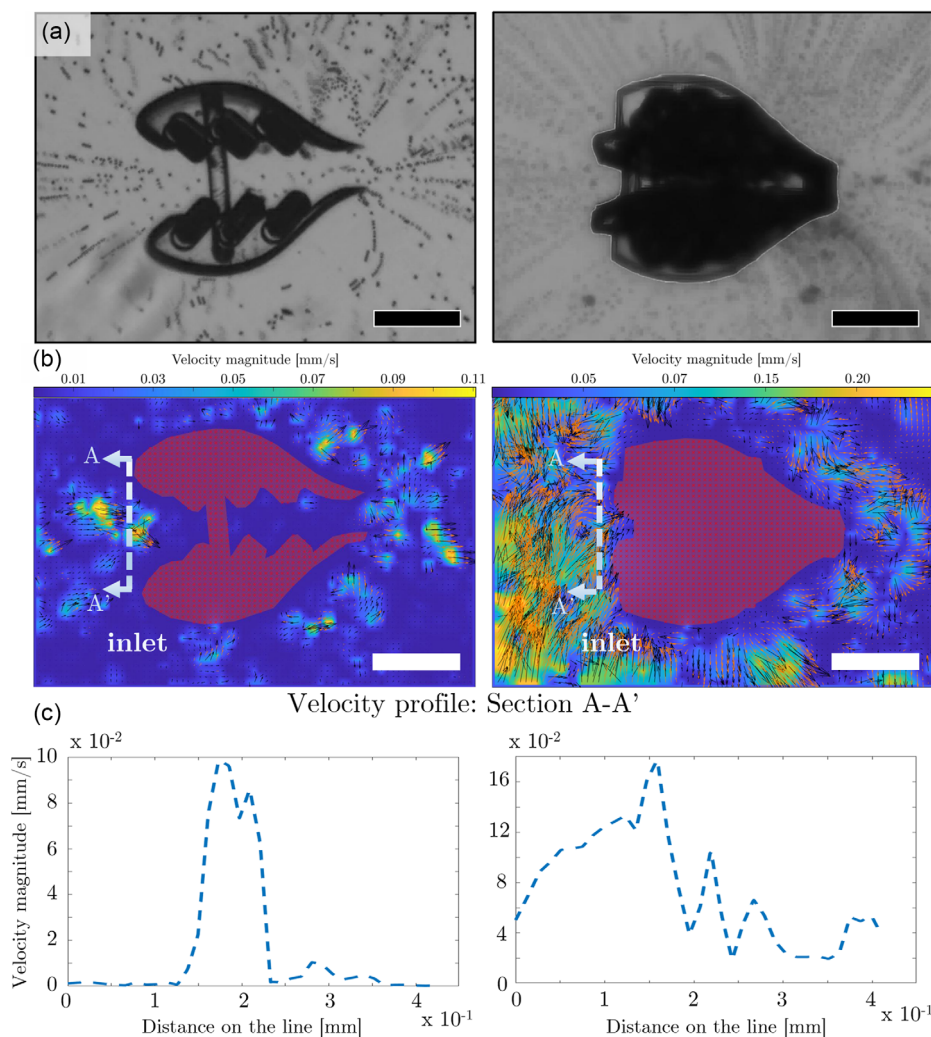


Figure 5. a) Superimposed time-lapse images showing the acoustic streaming pattern around microrobots with 6 and 18 oscillating microbubbles. b) Computation of the flow analysis using particle image velocimetry algorithm (PIVlab, MATLAB).^[38] A sectional line A–A' is selected at the inlet side of the microrobot to analyze the flow velocity magnitude profile of a selected frame. c) The flow velocity magnitude profile along the line A–A'. In the $n = 6$ case, the maximal flow velocity is 0.99 mm s^{-1} , whereas in the $n = 18$ case, the maximal flow velocity is 1.77 mm s^{-1} . This result shows that the acoustic streaming intensity can be strengthened in multibubble systems with a larger number of simultaneously oscillating bubbles. The x-axis from left to right corresponds to the section line from top to bottom in (b). Scale bars are $500 \mu\text{m}$.

different oscillatory modes at higher frequencies ($>80 \text{ kHz}$). This suggests that the hovering response of the microrobot is broadband with potentially higher harmonic resonance frequencies in the $80\text{--}100 \text{ kHz}$ range. Additionally, the bubbles show different modes of oscillations at these higher harmonics (Movie S2, Supporting Information). In the high-speed camera footages, we observe that these modes, specifically above 90 kHz , cause the bubble meniscus to lose contact with the pinning points of the cavity opening which could be detrimental to the stability of the entrapped bubbles and are thus less preferred range of actuation. Nevertheless, the vertical orientation and hovering mechanism are most consistently observed at 67 kHz and can be utilized to perform micromanipulation in remote environments.

2.4. Application as a Sample Extractor and Debris Clearance

Owing to the induced flow in the microrobot, alongside its hovering ability, we employ it as a miniaturized extractor to attract nearby particles and release them through its inner channel. The suction force generated at the wider end of the microrobot allows nearby particles to be pulled toward it from all directions and ejected away from the substrate up to several times the body length (Movie S4, Supporting Information). In the first demonstration, we show the microrobot hovering toward the debris of tracer microparticles and collecting them in two successive trials, at $t = 11 \text{ s}$ and $t = 14 \text{ s}$, respectively (Figure 6b). Moreover, the microrobot ejects the debris through its inner channel away from the substrate as this can be seen from the out-of-focus

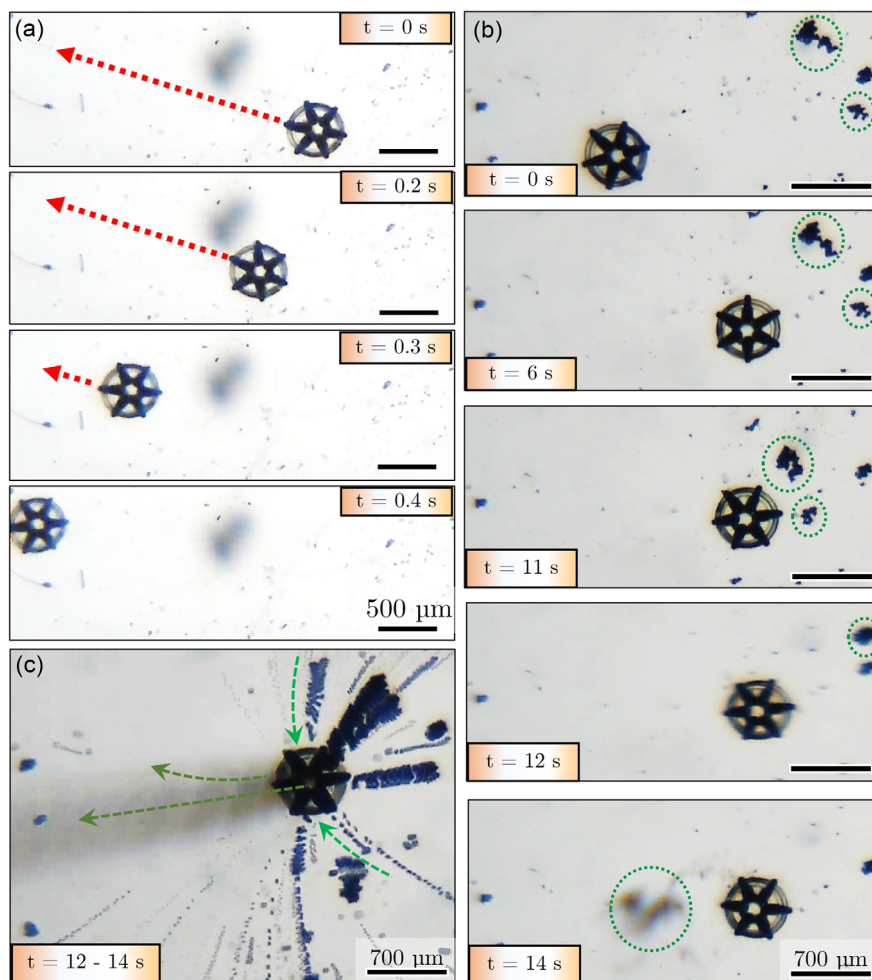


Figure 6. a) Hovering motion after the microrobot assumes vertical orientation (Movie S4, Supporting Information). Red arrows depict the direction of motion of the microrobot. b) Application of the microrobot as a μ -sieve where ($t = 0$ s) it approaches (in red) debris of microparticles (in green) of size $6 \mu\text{m}$, ($t = 6$ – 11 s) particles are pulled toward the microrobot due to the flow-induced suction, ($t = 12$ s) another cluster of debris is pulled toward the microrobot, and ($t = 14$ s) the second set of debris is ejected (Movie S4, Supporting Information). c) Superimposed time-lapse sequence ($t = 12$) showing debris of particles approaching the microrobot from all directions (dark green) and being released from the narrower end ($t = 14$, light green).

trajectories of cloud packets (Figure 6c, Movie S4, Supporting Information).

Second, we show the debris clearance functionality of our microrobot as it collects HeLa cell debris with flow-assisted suction created at its inlet. Typically, the preparation of cell cultures in biology requires flushing the workspace for the clearance of various kinds of cell debris such as dead cells and contaminants. In this experiment, we use the microrobot to demonstrate localized and selective debris clearance in a suspension containing dead HeLa cells and their cell spheroids. Under the acoustic actuation, the bubble oscillation-induced streaming attracts the HeLa cells toward the microrobot, filters them through the channel, and keeps some aggregated cells within the channel (Figure 7a). The retrieval of the microrobot can be achieved magnetically. We coat the microrobot with a thin layer of nickel using the physical vapor deposition process, which turns the surface of the microrobot magnetic which can be steered and thus retrieved with an external magnet^[15] (Movie S5, Supporting Information).

Compared to previously demonstrated applications of μ -sieves,^[30,39] the new design offers the advantage of on-site volumetric particle collection and clearance due to its 3D axisymmetric design. We envision this function of the microrobot to be useful for various applications that require remote access to biological or microfluidic workspaces for cleaning tasks e.g., endoscopic tools,^[18,40] tumor destruction and removal,^[41] and clearing dental pathways.^[42,43] Besides, the microrobot can offer an alternative for wastewater remediation^[31] or filtering of unwanted solid chemical wastes in fluids. Such applications of remediation using microrobots typically require either collective action of microrobots^[44] or enzymatic degradation of chemical waste.^[45]

3. Conclusions and Future Work

In this work, we present a new approach to design microrobots with a multi-bubble distribution inspired by the periodicity in

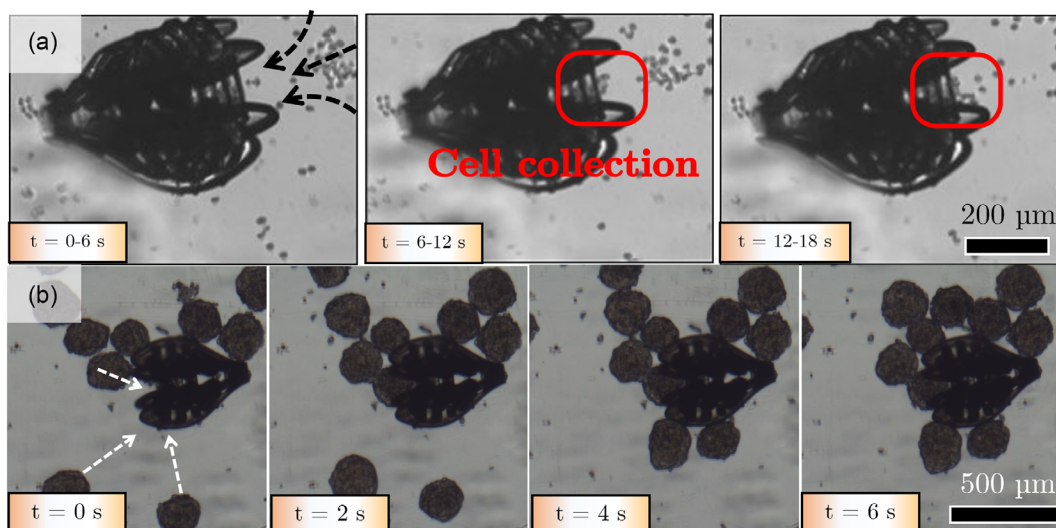


Figure 7. a) Superimposed time-lapse images of acoustic streaming assisted HeLa cells debris collection with the black arrows indicating the flow directions. The red rectangle marks the location where the HeLa cells are collected. The scale bar is 200 μm . b) Timestamps of acoustic microrobot collecting HeLa cells spheroids (diameter of 200 μm). The white dotted line arrows indicate the direction that the HeLa cell spheroids moving toward the microrobot. In these experiments, the microrobot is actuated at 67 kHz with a 20–40 V_{peak} driving signal. The scale bar is 500 μm .

metamaterials and powered by collective actuation of eighteen vibrating gas bubbles. We provide a comprehensive methodology based on high-speed imaging characterization of bubble oscillations of single cavity-entrapped bubbles that constitute the microrobot. Our work precipitates new research directions to design mesoscale robots that are easy to handle while keeping the benefits of microscale actuators. Specifically, the bubble-powered microrobots that are often limited by the lifetime of single bubbles as vibrating units could benefit from the use of large-bubble distributions inspired by their use as metamaterials.

With regard to the choice of cavity design, we study the oscillation amplitude and the lifetime of the bubbles trapped in different cavity opening geometries, ranging from fully open ($c = 100\%$) to half-open ($c = 50\%$). The requirement of the ideal bubble cavity design should allow larger bubble oscillation while retaining the bubbles for a longer duration of time. Hence, the $c = 75\%$ opened cavity is chosen in our final design considering both requirements. Next, we experimentally observe that the proposed microrobot shows a dominant streaming and subsequently hovering mechanism under acoustic actuation at 67 kHz, which does not strictly match the resonance frequency (Figure 3b) albeit closer to the predicted range. We also improved the contactless actuation of the acoustic microrobot with an immersible transducer, as opposed to piezoelectric-based workspaces, which makes it suitable for use in remote and inaccessible environments. The hovering action of the microrobot could benefit from directional steering attributed to the deposition of magnetic nanofilms, as shown in our previous work.^[15]

We also observe the hovering behavior to continue at higher frequencies ($\approx 70\text{--}90$ kHz) which can be attributed to possible higher order modes in this frequency range. Besides, our characterization studies also suggest that the bubbles show higher harmonic modes >80 kHz, where the oscillating bubble meniscus loses its pinning point at the cavity (Movie S2, Supporting

Information). Due to this high-frequency response, we avoid the actuation of the microrobot in the 80–90 kHz range despite their hovering response in this frequency range. Future studies may investigate the role of a shift in resonance frequency and modes of oscillations as different configurations of bubble distributions, akin to bubble-based metamaterials.^[21]

In terms of design, the microrobot can be appended with auxiliary units for particle collection or filtering, tailor-made for particle sorting as a μ -sieve. With regard to the performance, the induced flow can be further evaluated in terms of an increase in streaming-driven forces for higher bubble distributions than 18.^[20,24] Besides, future work includes the design of microrobots with different cavity designs that can be characterized as a mixed bubble distribution based on our approach. Here, cavities of different lengths and openings may provide insightful observations due to phase differences in their oscillatory behavior as they vibrate with different resonance frequencies. Such characterization studies offer new perspectives to design bubble-powered microrobots that benefit from multimodal operation with mixed resonance frequencies.

4. Experimental Section

Material and Fabrication: Both the microrobot and its representative cavity distributions are monolithic and made up of IP-Dip photoresist (Nanoscribe GmbH, Germany). They are 3D microprinted with DLW (Photonic GT2, Nanoscribe GmbH, Germany) using a 25 \times microscope objective. DLW is operated with the dip-in-laser lithography method. The microrobots are printed on an indium tin oxide-coated glass substrate in galvo-scanning mode with printing parameters described in prior works.^[11,15] The design features in the microrobot are optimized to the printing area, such that the overall lateral footprint (top view, Figure 1e) of the microrobot fits the DLW field (500 \times 500 μm) available for 25 \times objective. Importantly, the microrobots are fabricated using the z-drive printing mode, which allows printing along the z-direction (side

view, Figure 1b), as opposed to the traditionally allowed limit in Nanoscribe, i.e., 300 μm .

The cavity distributions for single bubble characterizations (Figure 3) are printed on the substrate such that the intercavity separation within the distribution is 1 mm to avoid cross-talk between the bubbles. For the investigation of streaming response, the microrobots are printed with their long axis parallel to the substrate. Following the 3D printing, the agents on the substrate are developed in 1-methoxy-2-propanol acetate for 25 min and rinsed in isopropyl alcohol for 5 min. Next, the substrate is postbaked on a hot plate at 150 °C for 5 min in order to remove the solvent residues. After development, the substrate surface is activated in an oxygen plasma chamber (50 W) for 40 s (Cute, Femto Science Inc., South Korea). The plasma treatment renders the surface of the micro-robot hydrophilic, such that no unwanted bubbles are formed around the body of the microrobot. During the acoustic actuation experiments, 10 μL of phosphate-buffered saline (1 \times) solution mixed with polystyrene tracer particles (6 μm diameter, Polysciences) is injected in proximity to the microrobot to visualize the acoustic streaming.

Instrumentation: The acoustic characterization setup comprised two configurations for (1) pressure measurements and high-speed imaging of single bubble-entrapped cavities, and (2) actuation of the microrobot and study of its hovering. The setup for (1) comprised a needle hydrophone (NH0200, Precision Acoustics, UK) connected to a preamplifier which led to a digital oscilloscope (PicoScope 3000 series, Pico Technology, UK) and finally read out as the electrical signal (in mV). The high-speed imaging setup comprised an illumination unit (swan neck optical, Mitutoyo, Japan) and a high-speed imaging camera (HPV-X2, Shimadzu, Japan). Detailed schematics for both pressure measurements and high-speed imaging setup are illustrated in Figure S1 and S2, Supporting Information. The setup for (2) comprised the ultrasonic transducer (PA1951, Precision Acoustics, UK) connected to a waveform generator (33510B, Keysight Inc., USA) whose driving signal is amplified up to 50 V_{peak} (PX200, PiezoDrive, Australia). The transducer is immersed in a water-filled acrylic tank and imaging using a light microscope (MF series, Mitutoyo, Japan) with a complementary metal–oxide–semiconductor camera (Point Grey Research, Inc., Blackfly GigE vision, pixel size = 3.75 μm) for real-time optical imaging.

Supporting Information

Supporting Information is available from the Wiley Online Library or from the author.

Acknowledgements

S.M. and Y.-H.L. contributed equally to this work. This work was supported by the European Research Council (ERC) under the European Union's Horizon 2020 Research and Innovation program under Grant 866494 project—MAESTRO.

Conflict of Interest

The authors declare no conflict of interest.

Data Availability Statement

The data that support the findings of this study are available from the corresponding author upon reasonable request.

Keywords

acoustic actuation, biomanipulation, bubbles, clinical ultrasound, metamaterials

Received: August 7, 2023

Revised: September 12, 2023

Published online: November 16, 2023

- [1] W. Chen, H. Zhou, B. Zhang, Q. Cao, B. Wang, X. Ma, W. Chen, H. Zhou, B. Zhang, X. Ma, Q. Cao, B. Wang, *Adv. Funct. Mater.* **2022**, *32*, 2110625.
- [2] D. Huang, L. Cai, N. Li, Y. Zhao, *Smart Med.* **2023**, *2*, e20230003.
- [3] S. Mohanty, Q. Jin, G. P. Furtado, A. Ghosh, G. Pahapale, I. S. M. Khalil, D. H. Gracias, S. Misra, *Adv. Intell. Syst.* **2020**, *2*, 2000064.
- [4] Y. Li, X. Liu, Q. Huang, A. T. Ohta, T. Arai, *Lab Chip* **2021**, *21*, 1016.
- [5] S. Mohanty, I. S. Khalil, S. Misra, *Proc. R. Soc. A* **2020**, *476*, 2243.
- [6] R. J. Dijkink, J. P. Van Der Dennen, C. D. Ohl, A. Prosperetti, *J. Micromech. Microeng.* **2006**, *16*, 1653.
- [7] D. Ahmed, C. Dillinger, A. Hong, B. J. Nelson, *Adv. Mater. Technol.* **2017**, *2*, 1700050.
- [8] A. Aghakhani, A. Pena-Francesch, U. Bozuyuk, H. Cetin, P. Wrede, M. Sitti, *Sci. Adv.* **2022**, *8*, 5126.
- [9] J. M. McNeill, N. Nama, J. M. Braxton, T. E. Mallouk, *ACS Nano* **2020**, *14*, 7520.
- [10] M. Kaynak, A. Dolev, M. S. Sakar, *Soft Rob.* **2023**, *10*, 246.
- [11] S. Mohanty, J. Zhang, J. M. McNeill, T. Kuenen, F. P. Linde, J. Rouwkema, S. Misra, *Sens. Actuators, B* **2021**, *347*, 130589.
- [12] F. W. Liu, S. K. Cho, *Lab Chip* **2021**, *21*, 355.
- [13] A. Dolev, M. Kaynak, M. S. Sakar, *Phys. Fluids* **2022**, *34*, 012012.
- [14] J. Xu, H. Cai, Z. Wu, X. Li, C. Tian, Z. Ao, V. C. Niu, X. Xiao, L. Jiang, M. Khodoun, M. Rothenberg, K. Mackie, J. Chen, L. P. Lee, F. Guo, *Nat. Commun.* **2023**, *14*, 869.
- [15] S. Mohanty, A. Paul, P. M. Matos, J. Zhang, J. Sikorski, S. Misra, *Small* **2022**, *18*, 2105829.
- [16] M. V. Patel, I. A. Nanayakkara, M. G. Simon, A. P. Lee, *Lab Chip* **2014**, *14*, 3860.
- [17] N. Garg, T. M. Westerhof, V. Liu, R. Liu, E. L. Nelson, A. P. Lee, *Microsyst. Nanoeng.* **2018**, *4*, 1.
- [18] T. Qiu, F. Adams, S. Palagi, K. Melde, A. Mark, U. Wetterauer, A. Miernik, P. Fischer, *ACS Appl. Mater. Interfaces* **2017**, *9*, 42536.
- [19] T. Combriat, P. Rouby-Poizat, A. A. Doinikov, O. Stephan, P. Marmottant, *Soft Matter* **2020**, *16*, 2829.
- [20] R. Goyal, A. G. Athanassiadis, Z. Ma, P. Fischer, *Phys. Rev. Lett.* **2022**, *128*, 254502.
- [21] Z. Cai, S. Zhao, Z. Huang, Z. Li, M. Su, Z. Zhang, Z. Zhao, X. Hu, Y. S. Wang, Y. Song, *Adv. Funct. Mater.* **2019**, *29*, 51.
- [22] Y. Zhou, L. Dai, N. Jiao, S. Zhang, Y. Zhou, L. Dai, N. Jiao, *Micromachines* **2022**, *13*, 1068.
- [23] T. Qiu, S. Palagi, A. G. Mark, K. Melde, F. Adams, P. Fischer, *Appl. Phys. Lett.* **2016**, *109*, 191602.
- [24] Z. Huang, S. Zhao, M. Su, Q. Yang, Z. Li, Z. Cai, H. Zhao, X. Hu, H. Zhou, F. Li, J. Yang, Y. Wang, Y. Song, *ACS Appl. Mater. Interfaces* **2020**, *12*, 1757.
- [25] S. A. Cummer, J. Christensen, A. Alù, *Nat. Rev. Mater.* **2016**, *1*, 1.
- [26] B. Assouar, B. Liang, Y. Wu, Y. Li, J. C. Cheng, Y. Jing, *Nat. Rev. Mater.* **2018**, *3*, 460.
- [27] J. Zhan, Y. Mei, K. Li, Y. Zhou, J. Chen, Y. Ma, *Appl. Phys. Lett.* **2022**, *120*, 094104.

- [28] A. Aghakhani, O. Yasa, P. Wrede, M. Sitti, *Proc. Natl. Acad. Sci. U. S. A.* **2020**, *117*, 3469.
- [29] H. Reinten, Y. Jethani, A. Fraters, R. Jeurissen, D. Lohse, M. Versluis, T. Segers, *J. Acoust. Soc. Am.* **2022**, *151*, 2545.
- [30] M. Kaynak, P. Dirix, M. S. Sakar, *Adv. Sci.* **2020**, *7*, 2001120.
- [31] Y. Ying, A. M. Pourrahimi, Z. Sofer, S. Matějková, M. Pumera, *ACS Nano* **2019**, *13*, 11477.
- [32] V. Liimatainen, D. M. Drotlef, D. Son, M. Sitti, *Adv. Mater.* **2020**, *32*, 2000497.
- [33] N. Bertin, T. A. Spelman, O. Stephan, L. Gredy, M. Bouriau, E. Lauga, P. Marmottant, *Phys. Rev. Appl.* **2015**, *4*, 064012.
- [34] S. Mohanty, R. J. Fidder, P. M. Matos, C. M. Heunis, M. Kaya, N. Blanken, S. Misra, *IEEE Trans. Ultrason. Ferroelectr. Freq. Control* **2022**, *69*, 988.
- [35] H. N. Oguz, A. Prosperetti, *J. Acoust. Soc. Am.* **1998**, *103*, 3301.
- [36] D. L. Miller, W. L. Nyborg, *J. Acoust. Soc. Am.* **1983**, *73*, 1537.
- [37] N. Mobadersany, K. Sarkar, *J. Fluid Mech.* **2019**, *875*, 781.
- [38] W. Thielicke, R. Sonntag, *J. Open Res. Software* **2021**, *9*, 12.
- [39] S. Hermanová, M. Pumera, *ACS Nanosci. Au* **2022**, *2*, 225.
- [40] M. Lee, G. Li, H. Li, X. Duan, M. B. Birla, T. S. Chang, D. K. Turgeon, K. R. Oldham, T. D. Wang, *Sci. Rep.* **2022**, *12*, 20155.
- [41] T. Gwisai, N. Mirkhani, M. G. Christiansen, T. T. Nguyen, V. Ling, S. Schuerle, *Sci. Rob.* **2022**, *7*, eabo0665.
- [42] N. Vyas, Q. X. Wang, K. A. Manmi, R. L. Sammons, S. A. Kuehne, A. D. Walmsley, *Ultrason. Sonochem.* **2020**, *67*, 105112.
- [43] T. Yamashita, K. Ando, *Ultrason. Sonochem.* **2019**, *52*, 268.
- [44] G. Gardi, S. Ceron, W. Wang, K. Petersen, M. Sitti, *Nat. Commun.* **2022**, *13*, 2239.
- [45] F. Soto, M. A. Lopez-Ramirez, I. Jeerapan, B. Esteban-Fernandez de Avila, R. K. Mishra, X. Lu, I. Chai, C. Chen, D. Kupor, A. Nourhani, J. Wang, *Adv. Funct. Mater.* **2019**, *29*, 1900658.
- [46] V. Leroy, A. Bretagne, M. Fink, H. Willaime, P. Tabeling, A. Tourin, *Appl. Phys. Lett.* **2009**, *95*, 17.
- [47] A. Bretagne, A. Tourin, V. Leroy, *Appl. Phys. Lett.* **2011**, *99*, 22.